Absence of density of states transfer observed by interlayer tunneling spectroscopy in magnetic fields for Bi2Sr2CaCu2O8+delta

AUTHOR(S):

Anagawa, K; Yamada, Y; Watanabe, T; Suzuki, M

PHYSICAL REVIEW B **67**, 115124 (2003)

First-principle dynamical electronic characteristics of Al electromigration in the bulk, surface, and grain boundary

K. Doi, K. Iguchi, K. Nakamura, and A. Tachibana*
Department of Engineering Physics and Mechanics, Kyoto University, Kyoto 606-8501, Japan
(Received 18 March 2002; revised manuscript received 21 October 2002; published 26 March 2003)

Formulas for the driving force of electromigration have been presented using concepts of the tension density, the external force density, and the effective charge tensor density. The ''dynamic'' wind charge tensor density $\vec{Z}_{a\ \mathrm{dynamic\ wind}}(\mathbf{r})$ has been revealed over and above the conventional ''static'' wind charge tensor density $\vec{Z}_{a\ \mathrm{static\ wind}}(\mathbf{r})$. We have demonstrated the application of the concepts to electromigration reliability problems of ultralarge-scale integration devices where extremely high current densities should be maintained through ultrathin film interconnects. Quantum mechanical wave-packet propagation of an Al atom has been examined in some models of thin Al lines which contain atomic defects, using the first-principle electronic structure calculations under the periodic boundary condition. The dynamical electronic properties by our simulation have demonstrated the characteristic features of the $\vec{Z}_{a\ \mathrm{dynamic\ wind}}(\mathbf{r})$ in the course of the Al electromigration in the bulk, surface, and grain boundary.

DOI: 10.1103/PhysRevB.67.115124 PACS number(s): 71.10.−w, 02.70.Ns, 71.15.Mb, 73.20.−r

I. INTRODUCTION

Studies of electromigration have led to an important active field of research in both theoretical and experimental aspects particularly because it has been the key issue of the reliability of interconnecting lines in ultralarge-scale integration (ULSI) technology.[1–5] Surface, grain boundary, and interfacial electromigration are particularly relevant to the problem of electromigration in the interior of bulk metals. From the experimental results, it is considered that an adatom or vacancy moves along a surface, interface, or grain boundary and grow into a hillock or whisker on a surface to release the stress.[1–3,6] Migrations of solutes in Al alloy are also observed.[7,8] The electromigration is a consequence of the interaction of an electric current under the external electric field $\mathbf{E}_{\mathrm{ext}}(\mathbf{r})$ and the impurities.

In the theoretical study, Bosvieux and Friedel[9] broke new ground for treating the electron scattering force of electromigration. Das and Peierls,[10,11] Sorbello,[12–14] Landauer,[15,16] Lodder,[17,18] and co-workers have attacked to this problem with various methods. A complete review of the theoretical studies of electromigration has recently been published by Sorbello.[19]

The electromigration force $\mathbf{F}_a(\mathbf{r})$ for an atom a is composed of a direct force and a wind force. The direct force is proportional to the $\mathbf{E}_{\mathrm{ext}}(\mathbf{r})$, while the momentum transfer on the migrating atom from the electric current is the origin of the wind force. The discrimination of the two forces has conveniently been represented as effective charge, as so observed experimentally. The effective charge Z_a^* for atom a is then written as

$$Z_a^* = Z_{a\ \mathrm{direct}} + Z_{a\ \mathrm{wind}}, \tag{1}$$

where $Z_{a\ \mathrm{direct}}$ is the direct charge associated with the direct force and $Z_{a\ \mathrm{wind}}$ is the wind charge associated with the wind force.[17,18] Theoretical works have exclusively been concentrated on calculating the effective charge Z_a^*.

New concept for electromigration has been given by Tachibana[20] using the nonrelativistic limit of quantum electrodynamics (QED), where the *effective charge tensor density* $\vec{Z}_a(\mathbf{r})$ has been given. The migrating impurities tunnel as well as hop across the energy barrier, forming measurable current. The current of the migrating impurities are characterized by the magnitude and direction it carries, which is represented by the probability flux density $\mathbf{S}_a(\mathbf{r})$. The ratio of the change in $\mathbf{S}_a(\mathbf{r})$ to that in time, multiplied with the mass m_a defines the electromigration force density $\mathbf{F}_a(\mathbf{r})$:

$$m_a \frac{\partial}{\partial t} \mathbf{S}_a(\mathbf{r}) = \mathbf{F}_a^s(\mathbf{r}). \tag{2}$$

To measure Z_a^*, $\mathbf{E}_{\mathrm{ext}}(\mathbf{r})$ is scanned up and down, when $\mathbf{F}_a(\mathbf{r})$ shifts in step with $\mathbf{E}_{\mathrm{ext}}(\mathbf{r})$. The ratio of the change in $\mathbf{F}_a(\mathbf{r})$ to that in $\mathbf{E}_{\mathrm{ext}}(\mathbf{r})$ defines the effective charge tensor density $\vec{Z}_a^*(\mathbf{r})$:[20,21]

$$\vec{Z}_a^*(\mathbf{r}) e N_a(\mathbf{r}) = \frac{\partial \mathbf{F}_a^s(\mathbf{r})}{\partial \mathbf{E}_{\mathrm{ext}}(\mathbf{r})}, \tag{3}$$

where e is the elementary electric charge and $N_a(\mathbf{r})$ is the position probability density designating the position $\mathbf{r}$ at which the impurities are most likely to be found. If $\vec{Z}_a^*(\mathbf{r})$ is averaged over certain region of space, then it can be Z_a^* observed experimentally in that region.[20]

An ion core affected by the electromigration force is usually treated as a classical particle and the force is calculated with the Feynman-Hellmann theorem,[22] but we treat the ion core as a Gaussian wave packet and try to represent the interaction between that core and electrons. Our motivated concept is shown in Fig. 1. If an atom is represented as a classical particle, its position will be actually decided even though the atom is exposed to the electric current and $\mathbf{E}_{\mathrm{ext}}(\mathbf{r})$, but if an atom is treated as a wave function, its position under the electric current and $\mathbf{E}_{\mathrm{ext}}(\mathbf{r})$ will *not* be determined definitely, and moreover the ion core will be in-

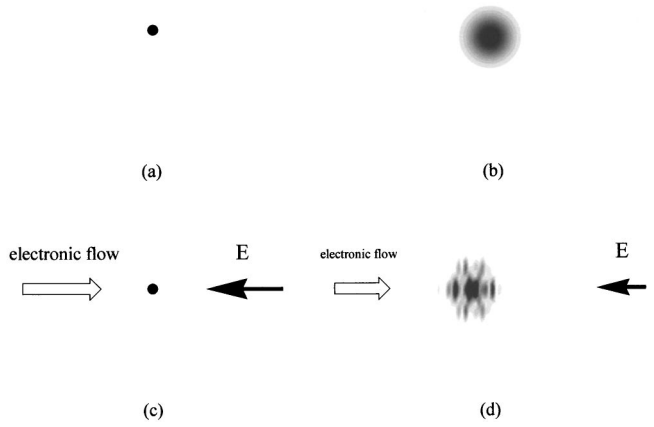

FIG. 1. Effect of electronic flow and $\mathbf{E}_{\mathrm{ext}}(\mathbf{r})$ on the electromigrating atom for (a) the dot as a material particle and (b) the cloud as a probability of a particle using the wave function. Under electronic flow and $\mathbf{E}_{\mathrm{ext}}(\mathbf{r})$, (c) the dot is not influenced by the change of environment, but (d) the cloud is caused the interference by the vibronic effect due to the wave functions of electrons in the electronic flow.

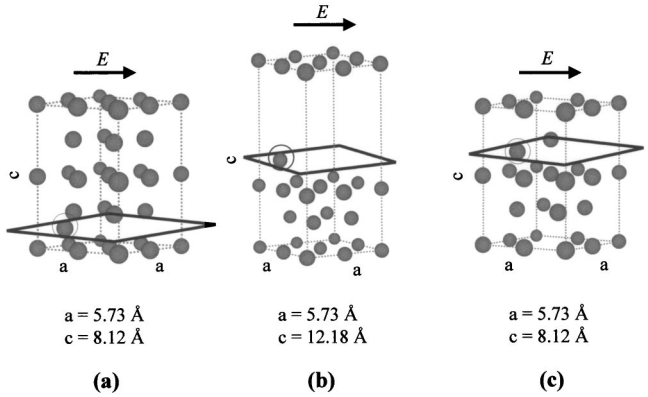

FIG. 2. Periodic models of electromigration in Al (100) surface for (a) bulk, (b) surface, and (c) grain boundary. Arrows point the direction of $\mathbf{E}_{\mathrm{ext}}(\mathbf{r})$, and squares inserted in the models indicate planes for maps in Figs. 6–11 on which the wave-packet ion core is put.

fluenced by the environment. In particular, the vibronic effect due to the wave functions of electrons in the electronic flow will cause the interference with the wave function of the ion core as shown in Fig. 1(d). The differentiation of the vibronic effect with respect to the electric field will have a direct bearing on the effective charge in any positions. We consider the interaction of the quantum core and electronic flow will represent interesting results.

We have reported the theoretical studies on the driving force of electromigration in Al systems.[20,23] In the first paper of the series, we have studied static electric properties of electromigrating systems as a function of surface orientations.[23] In the second, the dynamical properties has been formulated.[20] The underlying theory is the regional density functional theory[24] for the nonequilibrium dynamical processes,[25,26] and our interest here is the ''force'' on charged particles under ''dynamical'' as well as static conditions.[20,21,24–31] In the present paper, we shall apply the theory to the electromigration in some models of thin Al lines which contain the bulk, surface, and grain boundary, respectively, and try to discuss their electric properties. The unified treatment of the electromigration force and the effective charge will be shown.

II. COMPUTATIONAL METHOD

A. Models

Figure 2 shows the models of electromigration in an Al line for a bulk, surface, and grain boundary with periodic boundary condition. In these models an impurity is on a (001) plane in Al fcc structures and uniform $\mathbf{E}_{\mathrm{ext}}(\mathbf{r})$ is applied to the [110] direction. The bulk model [Fig. 2(a)] contains 16 Al atoms and an Al impurity in a unit cell. The unit cell has the base square with sides of 5.727 Å and the height 8.120 Å. The surface model [Fig. 2(b)] contains 12 Al atoms and an Al impurity in a unit cell. Its base size is the same as that of the bulk model and the height is 12.180 Å. In this model, the surface is the plane at 4.060 Å high from the base and the rest of the space is vacuum. The grain boundary model [Fig. 2(c)] contains 12 Al atoms and an Al atom in a unit cell. Its base size and height are the same as those of the bulk. In this model, a plane which should locate at 6.090 Å high from the base lacks and there is an atom from the upper layer. A grain boundary is a boundary between one structure and another in a crystal which is an assembly of a lot of grains. In this paper we made unstable region in the bulk model and called it the grain boundary model because of a restriction on the capacity for calculation. Electronic states of these models are calculated at room temperature of 302 K.

B. Wave-packet propagation

Quantum mechanical wave-packet propagation has been examined in each model by using the Bloch functions of electrons. Here, the density matrix of system $\hat{\rho}$ is defined by a direct product of that of an atom a, $\hat{\rho}_a$ and that of electrons $\hat{\rho}_e$ as follows:

$$\hat{\rho}=\hat{\rho}_a\otimes\hat{\rho}_e\,, \tag{4}$$

where

$$\hat{\rho}_a=|\psi_a(\mathbf{r})\rangle\langle\psi_a(\mathbf{r})|,$$

$$\hat{\rho}_e=\sum_j \nu_j|\psi_j(\mathbf{r}_e;\mathbf{r})\rangle\langle\psi_j(\mathbf{r}_e;\mathbf{r})|/N,\quad \sum_j \nu_j=N. \tag{5}$$

In this expression, $\psi_a(\mathbf{r})$ is the wave packet of an atom a, ν_j is the occupation number of the Bloch orbital $\psi_j(\mathbf{r}_e;\mathbf{r})$, where $j=n\mathbf{k}$ designates the band index n and crystal momentum $\mathbf{k}$, and N is the number of conducting electrons in a unit cell shown in Fig. 2. Bra and ket for $\psi_a(\mathbf{r})$ are performed the integral with respect to $\mathbf{r}$, and those for $\psi_j(\mathbf{r}_e;\mathbf{r})$ are done the integral with respect to the electron coordinate $\mathbf{r}_e$, where the integral region corresponds to the unit cell for both cases. The regional integral is designated as $\int_\Omega$ where Ω is the volume of the unit cell

$$\langle \psi_j(\mathbf{r}_e;\mathbf{r})|\psi_k(\mathbf{r}_e;\mathbf{r})\rangle = \int_\Omega \psi_j^*(\mathbf{r}_e;\mathbf{r})\psi_k(\mathbf{r}_e;\mathbf{r})d^3\mathbf{r}_e = \delta_{jk}, \quad (6)$$

where since the atomic motion is much slower than that of an electron, the $\psi_j(\mathbf{r}_e;\mathbf{r})$ is parametrically dependent on the atomic position $\mathbf{r}$ and orthonormalized with respect to $\mathbf{r}_e$. The wave function $\psi_j(\mathbf{r}_e;\mathbf{r})$ is expanded by plane waves

$$\psi_j(\mathbf{r}_e;\mathbf{r}) = \frac{1}{\sqrt{\Omega}}\sum_{\mathbf{G}} c_{\mathbf{G}} e^{i(\mathbf{k}+\mathbf{G})\cdot\mathbf{r}_e} \quad (7)$$

with

$$\sum_{\mathbf{G}} |c_{\mathbf{G}}|^2 = 1, \quad (8)$$

where $\cdot$ denotes inner product of vector. The wave packet ψ_a is also normalized and expanded by plane waves as follows:

$$\langle \psi_a(\mathbf{r})|\psi_a(\mathbf{r})\rangle = 1 \quad (9)$$

and

$$\psi_a(\mathbf{r}) = \frac{1}{\sqrt{\Omega}}\sum_{\mathbf{G}_a} c_{\mathbf{G}_a} e^{i(\mathbf{k}_a+\mathbf{G}_a)\cdot\mathbf{r}} \quad (10)$$

with

$$\sum_{\mathbf{G}_a} |c_{\mathbf{G}_a}|^2 = 1. \quad (11)$$

The ψ_a propagates in time according as

$$i\hbar\frac{d}{dt}c_{\mathbf{G}_a}(t) = \sum_{\mathbf{G}'_a} H_{\mathbf{G}_a\mathbf{G}'_a} c_{\mathbf{G}'_a}(t),$$
$$(c_{\mathbf{G}_a}(t)) = [e^{-(i/\hbar)H_{\mathbf{G}_a\mathbf{G}'_a}t}][c_{\mathbf{G}'_a}(0)], \quad (12)$$

with

$$H_{\mathbf{G}_a\mathbf{G}'_a} = \frac{\hbar^2}{2m_a}(\mathbf{k}_a+\mathbf{G}_a)^2\delta_{\mathbf{G}_a\mathbf{G}'_a} + \frac{1}{2}\Bigg[-i\frac{\hbar^2}{m_a}(\mathbf{k}_a+\mathbf{G}'_a)\cdot\int_\Omega d^3\mathbf{r}e^{i(\mathbf{G}'_a-\mathbf{G}_a)\cdot\mathbf{r}}\sum_j \frac{\nu_j}{N}\langle\psi_j(\mathbf{r}_e;\mathbf{r})|\nabla\psi_j(\mathbf{r}_e;\mathbf{r})\rangle$$
$$+i\frac{\hbar^2}{m_a}(\mathbf{k}_a+\mathbf{G}_a)\cdot\int_\Omega d^3\mathbf{r}e^{i(\mathbf{G}'_a-\mathbf{G}_a)\cdot\mathbf{r}}\sum_j \frac{\nu_j}{N}(\langle\psi_j(\mathbf{r}_e;\mathbf{r})|\nabla\psi_j(\mathbf{r}_e;\mathbf{r})\rangle)^*\Bigg]$$
$$-\frac{\hbar^2}{2m_\alpha}\int_\Omega d^3\mathbf{r}e^{i(\mathbf{G}'_a-\mathbf{G}_a)\cdot\mathbf{r}}\sum_j \frac{\nu_j}{N}\frac{1}{2}[\langle\psi_j(\mathbf{r}_e;\mathbf{r})|\Delta\psi_j(\mathbf{r}_e;\mathbf{r})\rangle + \text{c.c.}] + \int_\Omega d^3\mathbf{r}e^{i(\mathbf{G}'_a-\mathbf{G}_a)\cdot\mathbf{r}}U(\mathbf{r}), \quad (13)$$

where ∇ and Δ denote the gradient and the Laplacian with respect to $\mathbf{r}$, respectively. Uniform $\mathbf{E}_{\text{ext}}(\mathbf{r})$ of strength 1.0×10^{-4} in atomic unit (a.u.) (0.514 MV/cm) is contained in the potential $U(\mathbf{r})$. The initial state is set to be a simple Gaussian centered at $\mathbf{r}=\mathbf{R}_a$ in a unit cell

$$\psi_a(\mathbf{r}) = \left(\frac{2\zeta}{\zeta}\right)^{3/4} e^{i\mathbf{k}_a\cdot\mathbf{r}}\sum_{\mathbf{r}_p} e^{-\zeta(\mathbf{r}-\mathbf{R}_a-\mathbf{r}_p)^2}, \quad (14)$$

where $\mathbf{r}_p$ denotes the lattice translation vector

$$\mathbf{r}_p = n_x\mathbf{l}_x + n_y\mathbf{l}_y + n_z\mathbf{l}_z \quad (15)$$

with the unit lattice vectors $\mathbf{l}_x$, $\mathbf{l}_y$, and $\mathbf{l}_z$ and integers n_x, n_y, and n_z. The $\psi_a(\mathbf{r})$ is expanded by 1024 plane waves with

$$c_{\mathbf{G}_a} = N_a\left(\frac{2\pi}{\zeta}\right)^{3/4} e^{-i\mathbf{G}_a\cdot\mathbf{R}_a}e^{-|\mathbf{G}_a|^2/4\zeta}, \quad (16)$$

where N_a is normalization factor satisfying Eqs. (10) and (11).

C. Effective valence

The flux density $\mathbf{S}_a(\mathbf{r})$, the tension density $\boldsymbol{\tau}_a^S(\mathbf{r})$, and the external force density $\mathbf{K}_a^S(\mathbf{r})$ have been defined by Eqs. (36)–(38) in Ref. 20. The dynamic wind charge tensor density $\vec{Z}_{a\ \text{dynamic wind}}(\mathbf{r})$ and the static wind charge tensor density $\vec{Z}_{a\ \text{static wind}}(\mathbf{r})$ have been defined as follows:

$$\vec{Z}_{a\text{dynamic wind}}(\mathbf{r}) = \frac{1}{eN_a(\mathbf{r})}\frac{\partial\boldsymbol{\tau}_a^S(\mathbf{r})}{\partial\mathbf{E}_{\text{ext}}(\mathbf{r})} \quad (17)$$

and

$$\vec{Z}_{a\ \text{static wind}}(\mathbf{r}) = \frac{1}{eN_a(\mathbf{r})}\frac{\partial\mathbf{K}_a^S(\mathbf{r})}{\partial\mathbf{E}_{\text{ext}}(\mathbf{r})}. \quad (18)$$

The $\vec{Z}_{a\ \text{dynamic wind}}(\mathbf{r})$ has been calculated as follows:

$$\vec{Z}_{a\ \text{dynamic wind}}(\mathbf{r}) = \frac{\hbar^2}{4m_a\psi_a^*(\mathbf{r})\psi_a(\mathbf{r})}[\mathbf{z}_1(\mathbf{r})+\mathbf{z}_2(\mathbf{r})+\mathbf{z}_3(\mathbf{r})$$
$$+\mathbf{z}_4(\mathbf{r})+\mathbf{z}_5(\mathbf{r})+\mathbf{z}_6(\mathbf{r})]+\text{c.c.}, \quad (19)$$

where

$$z_1^k(\mathbf{r}) = 0, \quad (19a)$$

$$z_2^k(\mathbf{r}) = \psi_a^*(\mathbf{r})\Delta\psi_a(\mathbf{r})\sum_j\frac{1}{Ne}\frac{\partial\nu_j}{\partial\mathbf{E}_{\text{ext}}(\mathbf{r})}$$
$$\times\left[\left\langle\psi_j(\mathbf{r}_e;\mathbf{r})\left|\frac{\partial\psi_j(\mathbf{r}_e;\mathbf{r})}{\partial x^k}\right\rangle - \text{c.c.}\right], \quad (19b)$$

$$z_3^k(\mathbf{r}) = 2\left[\psi_a^*(\mathbf{r})\frac{\partial \nabla \psi_a(\mathbf{r})}{\partial x^k} - \frac{\partial \psi_a^*(\mathbf{r})}{\partial x^k}\nabla\psi_a(\mathbf{r})\right] \cdot \sum_j \frac{1}{Ne}\frac{\partial \nu_j}{\partial \mathbf{E}_{\mathrm{ext}}(\mathbf{r})}\langle \psi_j(\mathbf{r}_e;\mathbf{r})|\nabla\psi_j(\mathbf{r}_e;\mathbf{r})\rangle, \tag{19c}$$

$$z_4^k(\mathbf{r}) = 2\psi_a^*(\mathbf{r})\nabla\psi_a(\mathbf{r}) \cdot \sum_j \frac{1}{Ne}\frac{\partial \nu_j}{\partial \mathbf{E}_{\mathrm{ext}}(\mathbf{r})}\left[2\left\langle \psi_j(\mathbf{r}_e;\mathbf{r})\middle|\frac{\partial\nabla\psi_j(\mathbf{r}_e;\mathbf{r})}{\partial x^k}\right\rangle - \frac{\partial\langle \psi_j(\mathbf{r}_e;\mathbf{r})|\nabla\psi_j(\mathbf{r}_e;\mathbf{r})\rangle}{\partial x^k}\right], \tag{19d}$$

$$z_5^k(\mathbf{r}) = \left[\psi_a^*(\mathbf{r})\frac{\partial\psi_a(\mathbf{r})}{\partial x^k} - \frac{\partial\psi_a^*(\mathbf{r})}{\partial x^k}\psi_a(\mathbf{r})\right] \times \sum_j \frac{1}{Ne}\frac{\partial\nu_j}{\partial\mathbf{E}_{\mathrm{ext}}(\mathbf{r})}\langle\psi_j(\mathbf{r}_e;\mathbf{r})|\Delta\psi_j(\mathbf{r}_e;\mathbf{r})\rangle, \tag{19e}$$

$$z_6^k(\mathbf{r}) = \psi_a^*(\mathbf{r})\psi_a(\mathbf{r}) \times \sum_j \frac{1}{Ne}\frac{\partial\nu_j}{\partial\mathbf{E}_{\mathrm{ext}}(\mathbf{r})}\left[2\left\langle\psi_j(\mathbf{r}_e;\mathbf{r})\middle|\frac{\partial\Delta\psi_j(\mathbf{r}_e;\mathbf{r})}{\partial x^k}\right\rangle - \frac{\partial\langle\psi_j(\mathbf{r}_e;\mathbf{r})|\Delta\psi_j(\mathbf{r}_e;\mathbf{r})\rangle}{\partial x^k}\right]. \tag{19f}$$

The $\vec{Z}_{a\ \mathrm{static\ wind}}(\mathbf{r})$ has been calculated by assigning Z_a as the $Z_{a\ \mathrm{direct}}$ as

$$\vec{Z}_{a\ \mathrm{static\ wind}}(\mathbf{r}) = -\int_\Omega \sum_j \frac{1}{e}\frac{\partial\nu_j}{\partial\mathbf{E}_{\mathrm{ext}}(\mathbf{r})}\psi_j^*(\mathbf{r}_e;\mathbf{r})\psi_j(\mathbf{r}_e;\mathbf{r}) \times\nabla\left[\sum_{\mathbf{r}_p}\left(-\frac{Z_a e^2}{|\mathbf{r}_e-\mathbf{r}-\mathbf{r}_p|}\right)\right]d^3\mathbf{r}_e. \tag{20}$$

In both of these formulas, the change in occupation number has been estimated as

$$\delta\nu_{n\mathbf{k}} = e\tau_{n\mathbf{k}}\mathbf{E}_{\mathrm{ext}}(\mathbf{r})\cdot\mathbf{V}_{n\mathbf{k}}\partial f_0(\varepsilon_{n\mathbf{k}}-\varepsilon_F)/\partial\varepsilon_{n\mathbf{k}}, \tag{21}$$

where $\tau_{n\mathbf{k}}$ is the transport relaxation time of an electron with Bloch wave quantum number n and $\mathbf{k}$, f_0 is the Fermi distribution function, ε_F is the Fermi energy, and $\varepsilon_{n\mathbf{k}}$ and $\mathbf{V}_{n\mathbf{k}}$ are the energy and velocity of the electron. In this article, we have selected an excited-state configuration with a finite flux with carrying out the SCF procedure under the constraint that the Fermi surface is forced to shift. The calculus of variation with the constraint in this manner is based on the regional density functional theory[24] in the finite temperature encompassing nonequilibrium states,[25] chemical potentials,[26–28] and QED.[29–31] The shift of the Fermi surface was represented by taking $4\times4\times4$ k points with a shift of -0.05 fractional coordinate for each component of reciprocal lattice vector. Contribution to the relaxation was picked up from plane waves for valence electrons with short-range local relaxation in the equilibrium state, and the effect of core electrons was ignored. In this concept, we estimated $\mathbf{V}_{n\mathbf{k}}$ as $\mathbf{V}_{n\mathbf{k}}=1/\hbar(dT_{n\mathbf{k}}/d\mathbf{k})$, where $T_{n\mathbf{k}}$ is the electronic kinetic energy of nth band and wave vector $\mathbf{k}$, and approximate $\tau_{n\mathbf{k}}$ as the relaxation time τ for the Fermi surface. τ, which is satisfied with the equation

$$\frac{1}{\rho} = \frac{e^2\tau}{4\pi\hbar}\cdot\frac{1}{3}\int_{FS} dS_{n\mathbf{k}}\mathbf{V}_{n\mathbf{k}}, \tag{22}$$

where ρ is the resistivity and FS means the Fermi surface.[32] We have not found out the actual Fermi surface, so we approximate $\tau=100$ a.u. In Eq. (20) we put $Z_a=Z_{\mathrm{Al}}^{\mathrm{valence}}=3$ because of using pseudopotential for an Al atom which has three valence electrons. In this case an Al ion core is positive $(+3)$, but it is surrounded by electronic clouds under the excitation and relaxation processes which maintain the electric current. So we carried out the integration in Eq. (20) around the neighborhood of the core by finite numerical integration with 100 a.u. cutoff of $|\mathbf{r}_e-\mathbf{r}-\mathbf{r}_p|$. If an electron feels $+3$ charges of an Al core apart from infinite distance, then Eq. (20) should be calculated by Eq. (A4). Brackets for the electronic wave functions $\langle\psi_j(\mathbf{r}_e;\mathbf{r})|\partial\psi_j(\mathbf{r}_e;\mathbf{r})/\partial x^k\rangle$, in Eqs. (13) and (19) were estimated with the numerical differentiation with respect to the displacement of the atom a. The details of numerical calculations of this section are also shown in the Appendix of this paper.

III. RESULTS AND DISCUSSION

A. Wave-packet propagation

Figures 3–5, respectively, show the bulk, surface, and grain boundary models with an impurity ion core and snapshots of the wave-packet propagation for the core in each model. In these propagation, initially the wave-packet core has momentum $\hbar(9\times\pi/|\mathbf{l}_x|,9\times\pi/|\mathbf{l}_y|,1\times\pi/|\mathbf{l}_z|)$ a.u., which corresponds to about 11 m/s in velocity of the migration atom. The Gaussian wave packet is expanded by 1024 plane waves in Eqs. (10), (14), and (16) and propagated by Eqs. (12) and (13). We picked up pictures in which the density of the impurity appeared dense at local points. The initial momentum of the wave-packet core and the external electric field $\mathbf{E}_{\mathrm{ext}}$ are too large. In experimental data[1,2] the velocity of the migrating atom is about 10^{-9} m/s and current density is 10^6 A/cm^2. In our calculation current density $\mathbf{j}$ is estimated as 10^{12} A/cm^2, derived from $\mathbf{E}_{\mathrm{ext}}=\rho\cdot\mathbf{j}$ where the value of ρ is referred to Ref. 18. This wave-packet dynamics has lacked reality yet. However, our simulation by the wave-packet dynamics displays the diffusion on migrating process of Al atom qualitatively. It is found that the localization of the wave packet appears occasionally at different positions from the initial position as shown in (c)–(e) of Figs. 3–5, but there, the localization is too weak to discuss the effective charge. Therefore, in this paper, we shall report the results only of calculation using the initial wave packet, where the largest localization of the wave packet is observed.

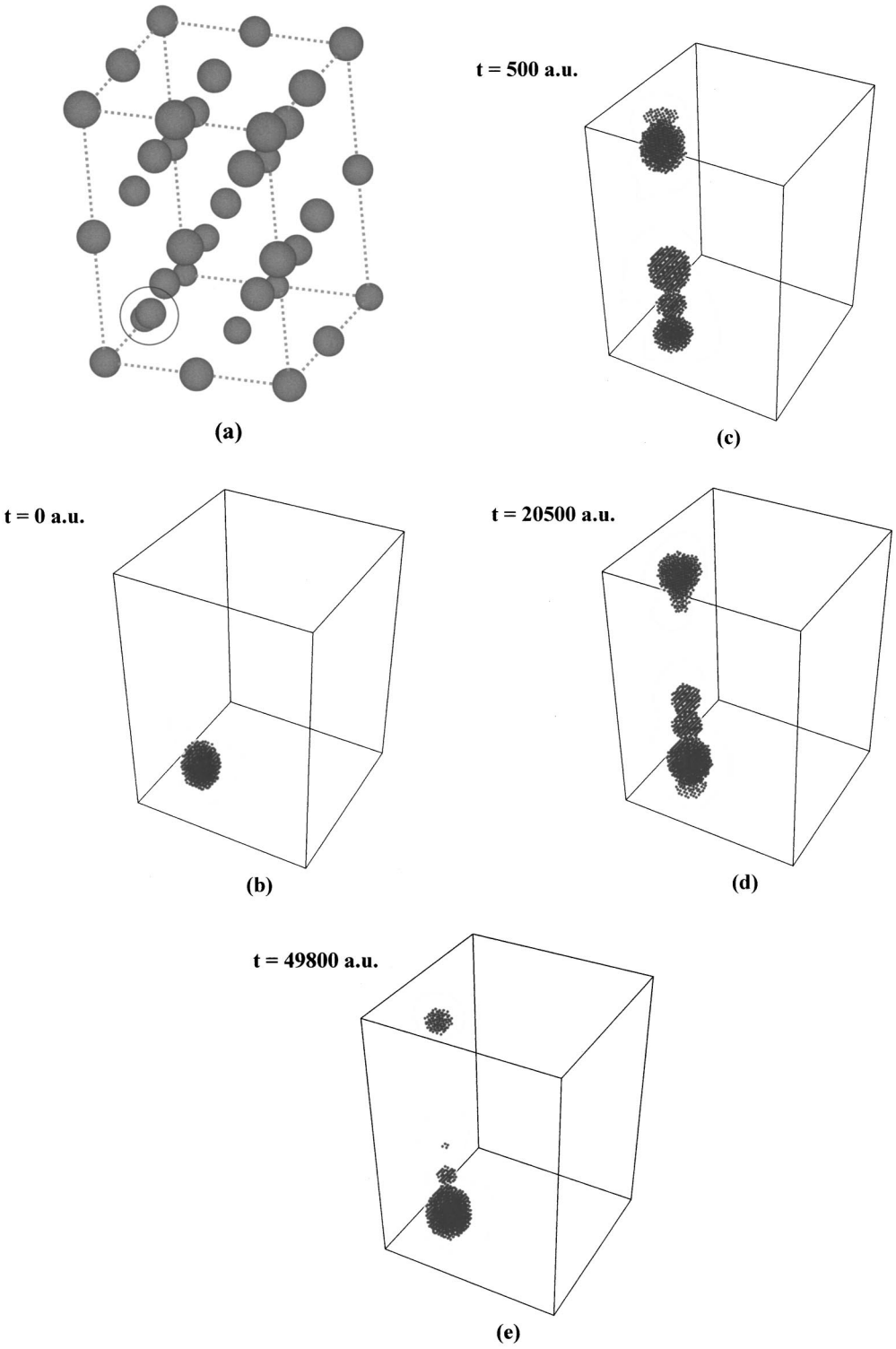

FIG. 3. The bulk model (a) contains an impurity in an open circle and (b), (c), (d), and (e) are snapshots of the wave-packet propagation. The snapshots picked up at time, (b) $t=0$, (c) $t=500$, (d) $t=20\,500$, and (e) $t=49\,800$ a.u., respectively. 1 a.u.$=2.42\times10^{-1}$ s.

B. Tension density and external force density

The tension density $\boldsymbol{\tau}^S_{\mathrm{Al}}(\mathbf{r})$ is defined by Eq. (37) in Ref. 20. $\boldsymbol{\tau}^S_{\mathrm{Al}}(\mathbf{r})$ is originated from the kinetic energy density of the ion core and electrons.[20] As shown in Fig. 6, $\boldsymbol{\tau}^S_{\mathrm{Al}}(\mathbf{r})$ on and around the wave-packet core is large and the direction is opposite to $\mathbf{E}_{\mathrm{ext}}(\mathbf{r})$, in the bulk, surface, and grain boundary, respectively.

The external force density $\mathbf{K}^S_{\mathrm{Al}}(\mathbf{r})$ balances with $\boldsymbol{\tau}^S_{\mathrm{Al}}(\mathbf{r})$ in the stationary state. As shown in Fig. 7, $\mathbf{K}^S_{\mathrm{Al}}(\mathbf{r})$ represents the interaction between the ion core and electrons. In the bulk,

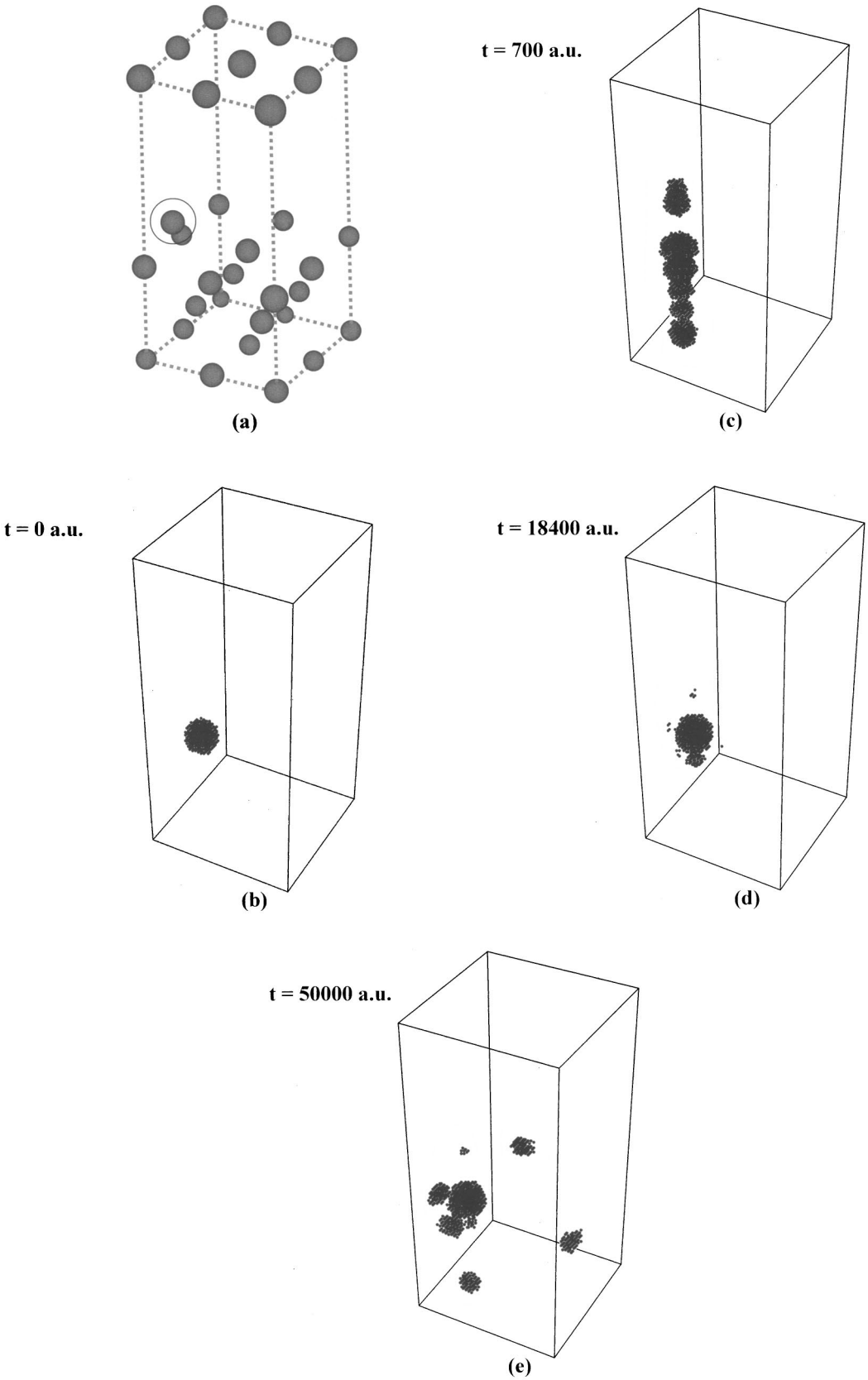

FIG. 4. The surface model (a) contains an impurity in an open circle and (b), (c), (d), and (e) are snapshots at time, (b) $t=0$, (c) $t=700$, (d) $t=18\,400$, and (e) $t=50\,000$ a.u., respectively.

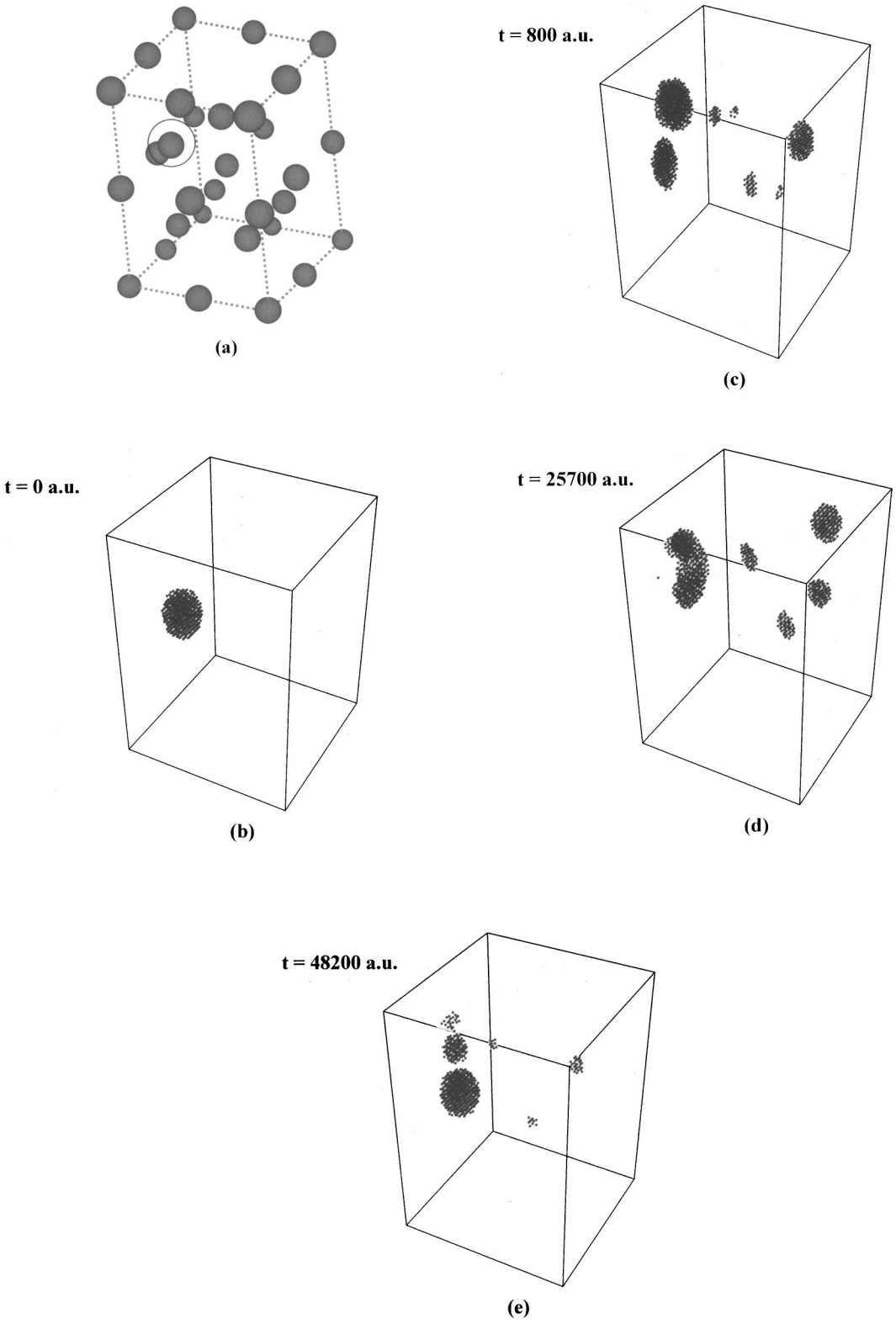

FIG. 5. The grain boundary model (a) contains an impurity in an open circle and (b), (c), (d), and (e) are snapshots at time, (b) $t=0$, (c) $t=800$, (d) $t=25\,700$, and (e) $t=48\,200$ a.u., respectively.

each $\mathbf{K}^S_{\mathrm{Al}}(\mathbf{r})$ around the core points the radial direction, but it concentrates on the similar direction to $\mathbf{E}_{\mathrm{ext}}(\mathbf{r})$ in the surface and grain boundary. Figure 8 shows the electromigration force density, that is, the sum of the external force density and the tension density. It is found that the magnitude of $\mathbf{K}^S_{\mathrm{Al}}(\mathbf{r})$ is larger than that of $\boldsymbol{\tau}^S_{\mathrm{Al}}(\mathbf{r})$ at most points, by the resemblance between Figs. 7 and 8 in each of the bulk, surface and grain boundary. It means that the external force

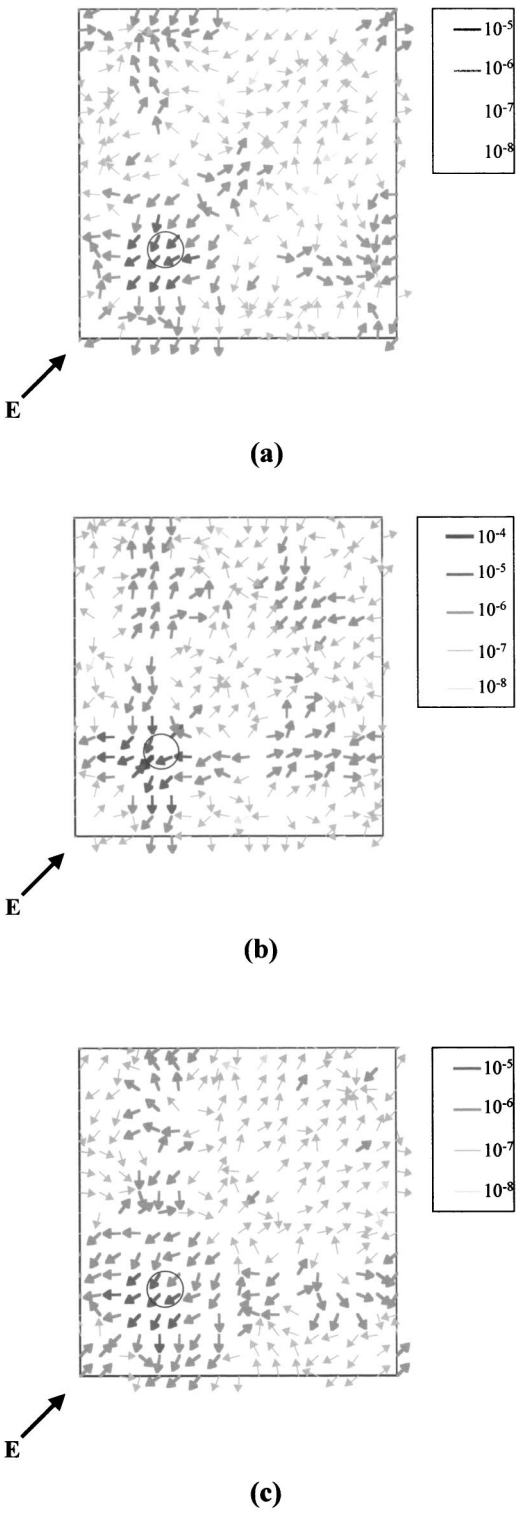

FIG. 6. Maps of the tension density $\boldsymbol{\tau}^S_{\mathrm{Al}}(\mathbf{r})$ for (a) bulk, (b) surface, and (c) grain boundary. The open circle shows the wave-packet core. The planes are referred to the squares in Fig. 2.

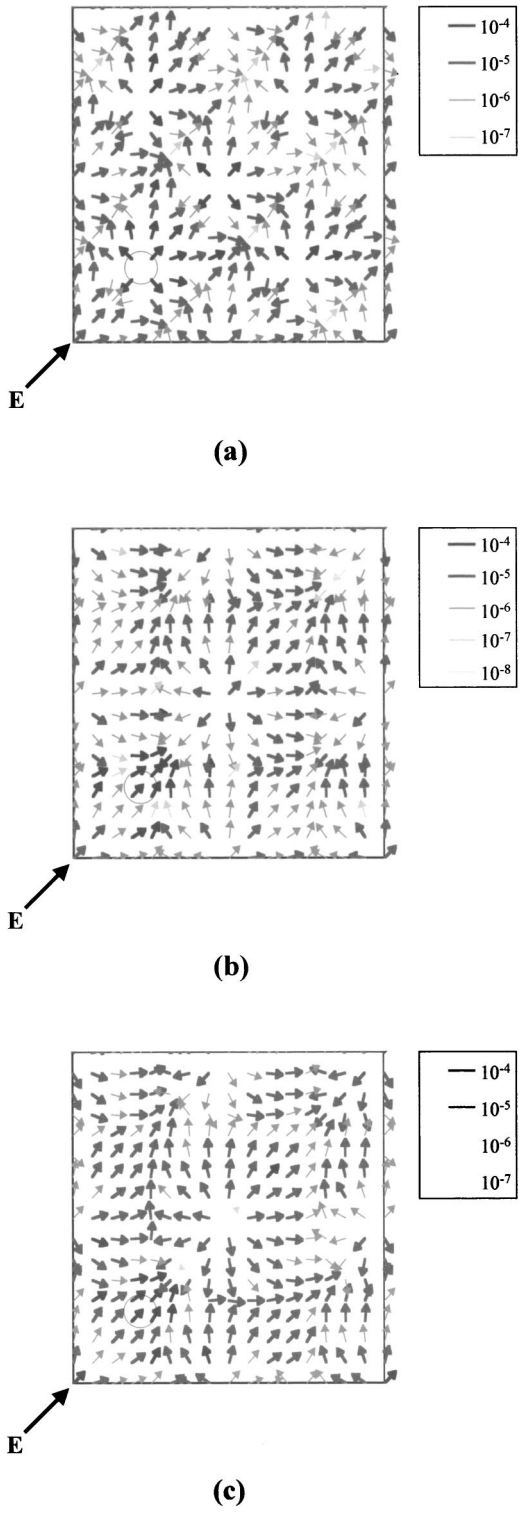

FIG. 7. Maps of the external force density $\mathbf{K}^S_{\mathrm{Al}}(\mathbf{r})$ for (a) bulk, (b) surface, and (c) grain boundary. The open circle shows the wave-packet core.

density seems to be dominant at most points. But on and around the wave-packet core, the effect of $\boldsymbol{\tau}^S_{\mathrm{Al}}(\mathbf{r})$ also appears clearly, since the magnitudes of $\mathbf{K}^S_{\mathrm{Al}}(\mathbf{r})$ and $\boldsymbol{\tau}^S_{\mathrm{Al}}(\mathbf{r})$ are the same order. Interesting force fields appear especially in the surface and grain boundary. The external force density on and around the wave-packet core point the similar direction to $\mathbf{E}_{\mathrm{ext}}(\mathbf{r})$, but the existence of $\boldsymbol{\tau}^S_{\mathrm{Al}}(\mathbf{r})$ changes the force direction. These two forces are particularly opposite to each other around the ion core.

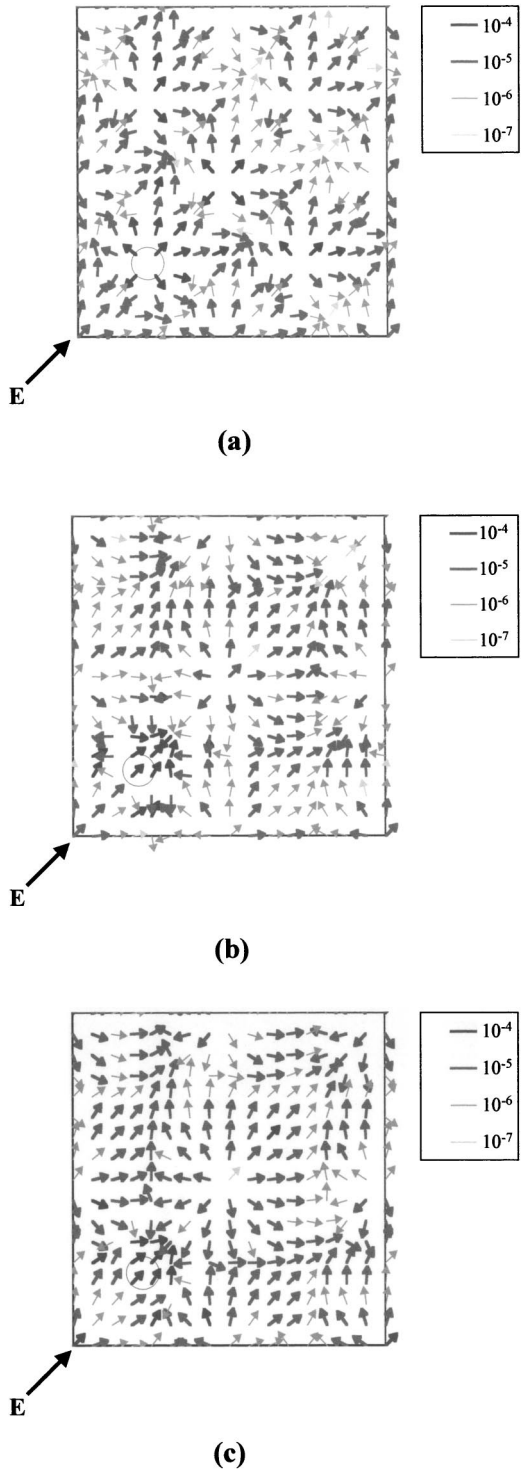

FIG. 8. Maps of the electromigration force density, which is the sum of the tension density $\boldsymbol{\tau}^S_{\mathrm{Al}}(\mathbf{r})$ and the external force density $\mathbf{K}^S_{\mathrm{Al}}(\mathbf{r})$, for (a) bulk, (b) surface, and (c) grain boundary. The open circle shows the wave-packet core.

C. Effective valence

The $\vec{Z}_{\text{Al dynamic wind}}(\mathbf{r})$ and the ratio $|\vec{Z}_{\text{Al dynamic wind}}(\mathbf{r})|/|\vec{Z}_{\text{Al static wind}}(\mathbf{r})|$ in models of the bulk, surface, and grain boundary of Al have been displayed together in Figs. 1–3 in Ref. 20, respectively. In this paper, we shall show the maps again with other components of wind charge, apart from the ratio $|\vec{Z}_{\text{Al dynamic wind}}(\mathbf{r})|/|\vec{Z}_{\text{Al static wind}}(\mathbf{r})|$. Figures 9 and 10 display the dynamic and static wind charges in models of the bulk, surface, and grain boundary of Al, respectively: also see Figs. 1–3 in Ref. 20. $\vec{Z}_{\text{Al dynamic wind}}(\mathbf{r})$ exceeds 10^3 in magnitude locally. This will predict some unknown phenomena in real systems. However, the average in space could be negligibly small. This interesting behavior should be originated from the null-sum rule of the tension density operator from which $\vec{Z}_{\text{Al dynamic wind}}(\mathbf{r})$ is derived; as shown in Eqs. (21) and (27) in Ref. 20. On the other hand, $\vec{Z}_{\text{Al static wind}}(\mathbf{r})$ has the conventional form of the Feynman-Hellmann theorem,[22] as shown in Eq. (28) in Ref. 20 and Eq. (20) in this paper. Accordingly, its average in space should be comparable to the value in theoretical literatures available.[9–17]

Comparing Figs. 9 and 10, $\vec{Z}_{\text{Al static wind}}(\mathbf{r})$ tends to be affected by $\mathbf{E}_{\text{ext}}(\mathbf{r})$ more easily than the $\vec{Z}_{\text{Al dynamic wind}}(\mathbf{r})$. As shown in Fig. 10, the direction of $\vec{Z}_{\text{Al static wind}}(\mathbf{r})$ is opposite to $\mathbf{E}_{\text{ext}}(\mathbf{r})$ in many points. However, $\vec{Z}_{\text{Al dynamic wind}}(\mathbf{r})$ does not indicate the particular direction such as $\vec{Z}_{\text{Al static wind}}(\mathbf{r})$. $\vec{Z}_{\text{Al static wind}}(\mathbf{r})$ is influenced by $\mathbf{E}_{\text{ext}}(\mathbf{r})$ more frequently in the surface and grain boundary than in the bulk. Large effective charge locally appears in the surface and the grain boundary. This result represents the properties of effective charge considered as a cause of wind force in electromigration. These results has not been reliable quantitatively yet but qualitatively agreed with experimental results which electromigration tend to occur more frequently in surfaces and grain boundaries.[1–4]

The total wind valence $\vec{Z}_{\text{Al wind}}(\mathbf{r})$ has been shown in Fig. 11. The ratio $|\vec{Z}_{\text{Al dynamic wind}}(\mathbf{r})|/|\vec{Z}_{\text{Al static wind}}(\mathbf{r})|$ is in the range from 10^{-1} to 10^2 and demonstrates significant figure at some characteristic points. In the bulk and the grain boundary the difference is apparent between the regions, governed by static wind charge and the dynamic wind charge. It is clear that these two kinds of charges depend on electronic properties around an impurity. The regions governed by static wind charge tend to be affected by $\mathbf{E}_{\text{ext}}$ and the characteristic properties appear in each model. In the bulk, effective charge points the opposite direction to $\mathbf{E}_{\text{ext}}$ in the area where the ratio $|\vec{Z}_{\text{Al dynamic wind}}(\mathbf{r})|/|\vec{Z}_{\text{Al static wind}}(\mathbf{r})|$ is small. In the surface, there is not so apparent difference between the regions in which static and dynamic wind charge is, respectively, dominant as in the bulk and the grain boundary. In the grain boundary, the effective charge does not opposite to $\mathbf{E}_{\text{ext}}$, even though in the region where the ratio $|\vec{Z}_{\text{Al dynamic wind}}(\mathbf{r})|/|\vec{Z}_{\text{Al static wind}}(\mathbf{r})|$ is small, because of the atom on the center of the plane, which causes the unstable structure. There is no significant correlation between the static wind charge and $\mathbf{E}_{\text{ext}}$ in this case. For the most part of the system, our results of the effective charge due to the wind force are too small, about 10^{-4} order of the results in references. It is caused by the underestimates of the vibronic effect in some reasons that range of the periodic boundary was

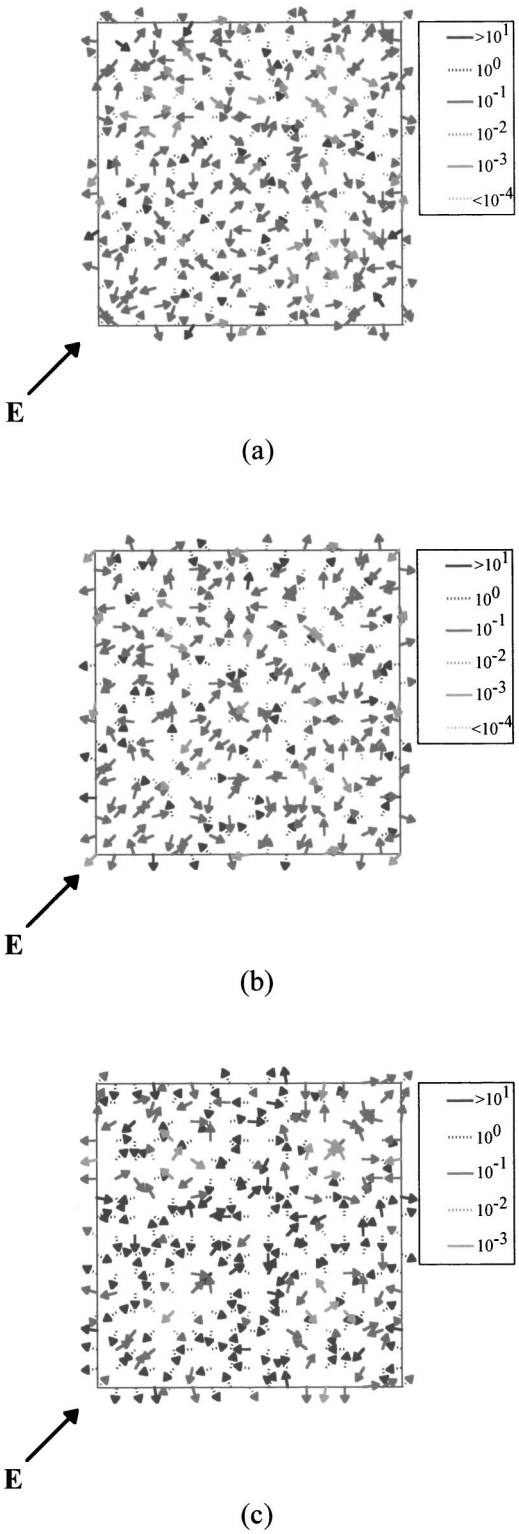

FIG. 9. Maps of the dynamic wind charge tensor density $\vec{\vec{Z}}_{\text{Al dynamic wind}}(\mathbf{r})$ for (a) bulk, (b) surface, and (c) grain boundary.

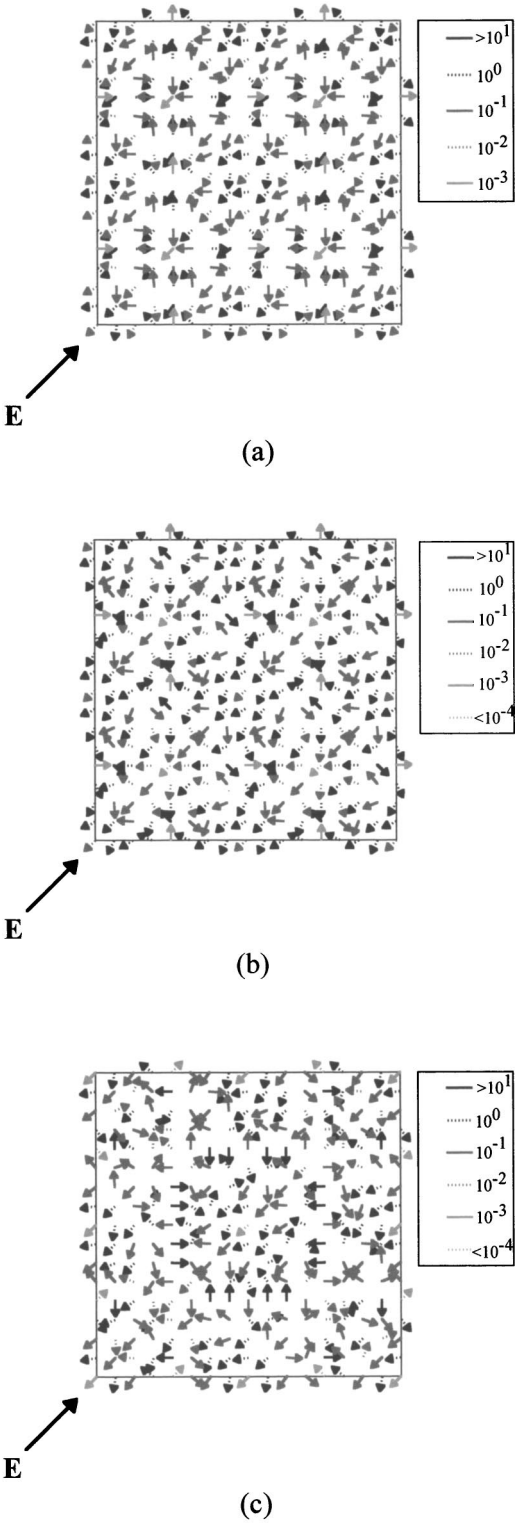

FIG. 10. Maps of the static wind charge tensor density $\vec{\vec{Z}}_{\text{Al static wind}}(\mathbf{r})$ for (a) bulk, (b) surface, and (c) grain boundary.

small, that effect of the external electric field on the electronic wave functions by the change in occupation number, Eq. (21), was insufficient, that the numerical estimates of $\langle \psi_j(\mathbf{r}_e;\mathbf{r}) | \partial \psi_j(\mathbf{r}_e;\mathbf{r})/\partial x^k \rangle$ were unreliable to some extent, and so on. However, our concepts and methodology of the first-principles dynamical electronic properties such as the dynamic wind force $\vec{\vec{Z}}_{\text{Al dynamic wind}}(\mathbf{r})$, are extremely valid for interconnecting systems.

Furthermore, we have calculated variants of the $\vec{\vec{Z}}_{\text{Al static wind}}(\mathbf{r})$ at some characteristic positions, where the ra-

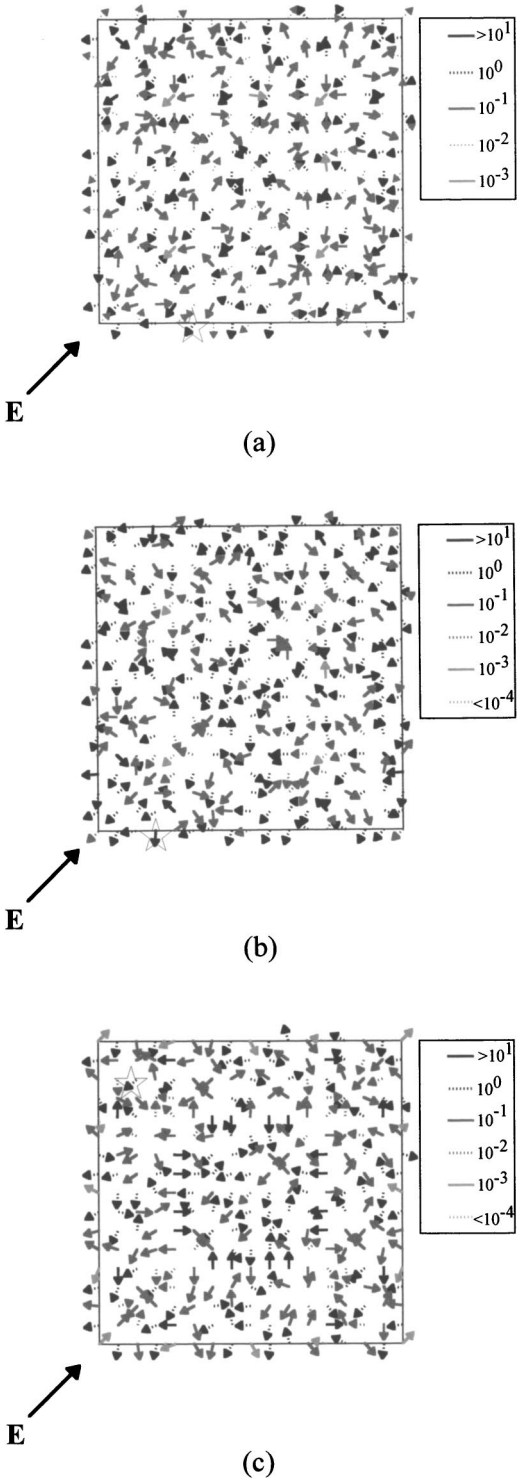

FIG. 11. Maps of the total wind charge tensor density $\vec{Z}_{\text{Al wind}}(\mathbf{r})$, which is composed of $\vec{Z}_{\text{Al dynamic wind}}(\mathbf{r})$ and $\vec{Z}_{\text{Al static wind}}(\mathbf{r})$ for (a) bulk, (b) surface, and (c) grain boundary. The star in the map denotes the position of calculating the effective charge in Table I.

tio $|\vec{Z}_{\text{Al dynamic wind}}(\mathbf{r})|/|\vec{Z}_{\text{Al static wind}}(\mathbf{r})|$ is large and the value of $\vec{Z}_{\text{Al static wind}}(\mathbf{r})$ is not so small. These positions are annotated by a star in Fig. 11.

First, we took the conventional method for calculation of the effective charge, which is based on the conductivity of band. Contribution to the relaxation was picked up from not only valence electrons but also core electrons with long-range relaxation in the equilibrium state as follows:

$$\vec{Z}'_{\text{Al static wind}}(\mathbf{r}) = -\int_{\Omega}\sum_{j}\frac{1}{e}\frac{\partial\nu_j}{\partial\mathbf{E}_{\text{ext}}(\mathbf{r})}\psi_j^*(\mathbf{r}_e;\mathbf{r})\psi_j(\mathbf{r}_e;\mathbf{r}) \times\nabla\left[\sum_{\mathbf{r}_p}\left(-\frac{Z_{\text{Al}}^{\text{valence}}e^2}{|\mathbf{r}_e-\mathbf{r}-\mathbf{r}_p|}+\nu_{\text{core}}(\mathbf{r}_e;\mathbf{r}+\mathbf{r}_p)\right)\right]d^3\mathbf{r}_e, \tag{23}$$

where ν_{core} is the potential of core electrons. In this variant, $\mathbf{V}_{n\mathbf{k}}$ in Eq. (21) was obtained by the group velocity of bands as $\mathbf{V}_{n\mathbf{k}}=1/\hbar(d\varepsilon_{n\mathbf{k}}/d\mathbf{k})$, and integrals in Eq. (23) were carried out analytically in accordance with Eq. (A4) in the Appendix.

Next, we have calculated the effective charge without using Eq. (21), that is, the effective charge was estimated directly by the differential of the SCF Hellmann-Feynman forces[22] for Al with respect to $\mathbf{E}_{\text{ext}}(\mathbf{r})$ in the right hand side of Eq. (18),

$$\vec{Z}''_{\text{Al static wind}}(\mathbf{r})=\frac{1}{e}\frac{\partial\mathbf{F}_{\text{Al}}^{\text{full}}(\mathbf{r})}{\partial\mathbf{E}_{\text{ext}}(\mathbf{r})} \tag{24}$$

and

$$\vec{Z}'''_{\text{Al static wind}}(\mathbf{r})=\frac{Z_{\text{Al}}^{\text{full}}}{Z_{\text{Al}}^{\text{valence}}}\frac{1}{e}\frac{\partial\mathbf{F}_{\text{Al}}^{\text{valence}}(\mathbf{r})}{\partial\mathbf{E}_{\text{ext}}(\mathbf{r})}, \tag{25}$$

where $\mathbf{F}_{\text{Al}}^{\text{full}}(\mathbf{r})$ is the Hellmann-Feynman force considering both core and valence electrons and $\mathbf{F}_{\text{Al}}^{\text{valence}}(\mathbf{r})$ is one considering only valence electrons. The differential can be numerical estimated by using a series of $\mathbf{F}_{\text{Al}}^{\text{full}}(\mathbf{r})$ or $\mathbf{F}_{\text{Al}}^{\text{valence}}(\mathbf{r})$ under $\mathbf{E}_{\text{ext}}(\mathbf{r})$ as noted in the Appendix. In particular, the latter Eq. (25) is considered the effective charge by taking account only of valence electrons with $Z_{\text{Al}}^{\text{full}}=13$.

Results of calculations are tabulated in Table I. According to the concepts, values of the static wind charge tensor density are different from one another. As compared with the results of the effective charge in Al bulk system with a defect by Lodder and Dekker,[18] our results of the static wind charge are extremely large despite the *pd* component of wave function has not been taken into account properly in the plane-wave expansion. However, on the points where the dynamic wind charge has influence as ones we selected, the static wind charge is put into the shade by the dynamic wind charge for any concepts we have set up. It means that consideration of the dynamical electronic properties is very important to analyze the driving force in electromigration.

IV. CONCLUSION

We have presented concepts of the first-principles dynamical electronic properties and applied our theory to

TABLE I. Diagonal element of the dynamic wind charge tensor density $\vec{Z}_{\text{Al dynamic wind}}(\mathbf{r})$ [Eq. (19); Fig. 9] and the static wind charge tensor densities $\vec{Z}_{\text{Al static wind}}(\mathbf{r})$ [Eq. (20); Fig. 10], $\vec{Z}'_{\text{Al static wind}}(\mathbf{r})$ [Eq. (23)], $\vec{Z}''_{\text{Al static wind}}(\mathbf{r})$ [Eq. (24)], and $\vec{Z}'''_{\text{Al static wind}}(\mathbf{r})$ [Eq. (25)] on the points annotated by a star in Fig. 11.

	Bulk [Fig. 11(a)]			
	x	y	z	norm
$\vec{Z}_{\text{Al dynamic wind}}(\mathbf{r})$	−5.1500	−8.3315	2.4882	10.1058
$\vec{Z}_{\text{Al static wind}}(\mathbf{r})$	−0.5424	0.6205	−2.4439	2.5791
$\vec{Z}'_{\text{Al static wind}}(\mathbf{r})$	−0.2411	0.1641	0.1178	0.3145
$\vec{Z}''_{\text{Al static wind}}(\mathbf{r})$	0.0467	−0.9217	0.0385	0.9237
$\vec{Z}'''_{\text{Al static wind}}(\mathbf{r})$	0.5775	3.9335	−0.5686	4.0162
	Surface [Fig. 11(b)]			
	x	y	z	norm
$\vec{Z}_{\text{Al dynamic wind}}(\mathbf{r})$	0.1863	−17.1430	5.6851	18.0621
$\vec{Z}_{\text{Al static wind}}(\mathbf{r})$	−1.3333	0.6259	7.7903	7.9283
$\vec{Z}'_{\text{Al static wind}}(\mathbf{r})$	0.6881	0.1145	1.9659	2.0860
$\vec{Z}''_{\text{Al static wind}}(\mathbf{r})$	−0.1815	−0.8098	0.2275	0.8605
$\vec{Z}'''_{\text{Al static wind}}(\mathbf{r})$	−1.0070	4.1659	−0.1322	4.2879
	Grain boundary [Fig. 11(c)]			
	x	y	z	norm
$\vec{Z}_{\text{Al dynamic wind}}(\mathbf{r})$	−6.1505	−5.4763	−0.8337	8.2773
$\vec{Z}_{\text{Al static wind}}(\mathbf{r})$	−0.1900	−0.1899	−3.5574	3.5675
$\vec{Z}'_{\text{Al static wind}}(\mathbf{r})$	0.3674	−0.7249	0.8433	1.1712
$\vec{Z}''_{\text{Al static wind}}(\mathbf{r})$	−0.2554	0.0285	−0.0020	0.2570
$\vec{Z}'''_{\text{Al static wind}}(\mathbf{r})$	−0.3472	6.8023	0.1483	6.8128

the electromigrating Al systems by means of wave-packet propagation.

Electromigration force has been formulated using the nonrelativistic limit of QED. *Tension density* emerges from the viewpoint of ''action through medium'' in the quantum field theory rather than ''action at a distance.'' Furthermore, *dynamic wind charge* has been revealed over and above the conventional static wind charge and the direct charge. The dynamic wind charge reflects the dynamic interchange of momentums between conducting electrons and migrating atoms.

Quantum mechanical wave-packet propagation has been examined in some models of thin Al lines which contain the bulk, surface, and grain boundary, respectively, using first-principle electronic structure calculations with periodic boundary condition. This wave-packet dynamics has lacked reality yet. However, our simulation by the wave-packet dynamics displays the diffusion on migrating process of Al atom qualitatively. It is found that the localization of the wave packet appears occasionally at different positions from the initial position, but there, the localization is too weak to discuss the effective charge. Therefore, in this paper, we shall report the results only of calculation using the initial wave packet, where the largest localization of the wave packet is observed. We have calculated the tension density, the external force density, and the effective charge tensor density due to dynamic and static wind force. We divided the force density on an impurity into tension density due to the kinetic energy density[20] and external force density due to the potential energy, and we got effective charge tensor density from the two kinds of force densities. These properties display different features according to the character of system. In particular, the dynamic wind charge demonstrates significant figure at some characteristic points. Our concepts and methodology of the first-principle dynamical electronic properties are extremely valid for interconnecting systems, and we have continued improvement of the algorithm computing these dynamical electronic properties.

ACKNOWLEDGMENTS

This work has been supported by Grant-in-Aid for Scientific Research from the Ministry of Education, Science and Culture of Japan, for which we express our gratitude.

APPENDIX

Bloch wave functions in this study have been determined by first-principles electronic structure calculations based on density functional theory, using the pseudopotential method and generalized-gradient approximation by Perdew and Wang.[33,34] For the calculation of potential $U(\mathbf{r})$ in Eq. (13), cutoff energy is adopted to 30 Rydberg (408 eV) using 16 k points with 40×40×56 (for the bulk and grain boundary) and 40×40×84 (for the surface) FFT grids. The choice of k points is according to the scheme proposed by Monkhorst and Pack.[35] Except for the calculation of $U(\mathbf{r})$, we took 64 k points with a shift of −0.05 fractional coordinate for each component of reciprocal lattice vector.

Brackets for the electronic wave functions $\langle \psi_j(\mathbf{r}_e;\mathbf{r}) | \partial\psi_j(\mathbf{r}_e;\mathbf{r})/\partial x^k \rangle$, in Eqs. (13) and (19) were estimated with the numerical differentiation of the overlap between plane waves containing deviation of displacement of the atom a as follows:

$$\left\langle \psi_j(\mathbf{r}_e;\mathbf{r}) \left| \frac{\partial\psi_j(\mathbf{r}_e;\mathbf{r})}{\partial x^k} \right\rangle \right. = \frac{\langle \psi_j(\mathbf{r}_e;\mathbf{r}) | \psi_j(\mathbf{r}_e;\mathbf{r}+\Delta x^k)\rangle - \langle \psi_j(\mathbf{r}_e;\mathbf{r}) | \psi_j(\mathbf{r}_e;\mathbf{r}-\Delta x^k)\rangle}{2\Delta x^k}, \tag{A1}$$

with $\Delta x^k = 0.001$ a.u. Brackets in the right hand of Eq. (A1) were calculated by analytical integration.

In the concept that contribution to the relaxation was picked up only from plane waves for valence electrons with short-range local relaxation in the equilibrium state, we assumed that the electronic velocity $\mathbf{V}_{n\mathbf{k}}$ is given by using the noninteracting electronic kinetic energy of nth band and wave vector $\mathbf{k}$, $T_{n\mathbf{k}}$, as follows:

$$V^x_{n,\mathbf{k}} = \frac{T_{n,\mathbf{k}+\Delta\mathbf{k}} - T_{n,\mathbf{k}-\Delta\mathbf{k}}}{2\hbar\Delta k_x}, \quad V^y_{n,\mathbf{k}} = \frac{T_{n,\mathbf{k}+\Delta\mathbf{k}} - T_{n,\mathbf{k}-\Delta\mathbf{k}}}{2\hbar\Delta k_y},$$

$$V^z_{n,\mathbf{k}} = \frac{T_{n,\mathbf{k}+\Delta\mathbf{k}} - T_{n,\mathbf{k}-\Delta\mathbf{k}}}{2\hbar\Delta k_z}, \tag{A2}$$

with

$$T_{n,\mathbf{k}} = -\frac{\hbar^2}{2m_e}\langle\psi_{n,\mathbf{k}}(\mathbf{r}_e;\mathbf{r})|\Delta\psi_{n,\mathbf{k}}(\mathbf{r}_e;\mathbf{r})\rangle, \tag{A3}$$

where m_e is the mass of electron. In this paper, Δk_x, Δk_y, and Δk_z correspond to a fourth of each component of the unit reciprocal lattice vector.

If an Al core has a constant charge wherever electrons exist, then integrals in Eq. (19) should be calculated as follows:

$$\int_\Omega \psi_j^*(\mathbf{r}_e;\mathbf{r})\psi_j(\mathbf{r}_e;\mathbf{r})\nabla\left[\sum_{\mathbf{r}_p}\left(-\frac{Z_a e^2}{|\mathbf{r}_e-\mathbf{r}-\mathbf{r}_p|}\right)\right]d^3\mathbf{r}_e$$
$$= \frac{4\pi Z_a e^2}{\Omega}\sum_{\mathbf{G},\mathbf{G}'} c^*_{\mathbf{G}'}c_{\mathbf{G}}\frac{i(\mathbf{G}'-\mathbf{G})}{|\mathbf{G}'-\mathbf{G}|^2}e^{-i(\mathbf{G}'-\mathbf{G})\cdot\mathbf{r}}. \tag{A4}$$

In order to calculate the relaxation time τ, we must integrate electronic velocity $\mathbf{V}_{n\mathbf{k}}$ on the Fermi surface in Eq. (22). But the number of k points has not been sufficient to calculate Eq. (22). Contrary to procedures by Eqs. (19)–(23), the relaxation time can be contained implicitly, according to the Bloch wave quantum number n and $\mathbf{k}$, in the differential with respect to $\mathbf{E}_{\text{ext}}(\mathbf{r})$ in Eqs. (24) and (25). Equation (25) can be introduced by the transformation of Eq. (24) as follows:

$$\begin{aligned}
\vec{Z}''_{\text{Al static wind}}(\mathbf{r}) &= \frac{1}{e}\frac{\partial\mathbf{F}^{\text{full}}_{\text{Al}}(\mathbf{r})}{\partial\mathbf{E}_{\text{ext}}(\mathbf{r})} = \frac{\partial}{\partial\mathbf{E}_{\text{ext}}(\mathbf{r})}\left\{-\int_\Omega\sum_j^{\text{valence}}\frac{1}{e}\nu_j\psi_j^*(\mathbf{r}_e;\mathbf{r})\psi_j(\mathbf{r}_e;\mathbf{r})\nabla\left[\sum_{\mathbf{r}_p}\left(-\frac{Z^{\text{valence}}_{\text{Al}}e^2}{|\mathbf{r}_e-\mathbf{r}-\mathbf{r}_p|}+\nu_{\text{core}}(\mathbf{r}_e;\mathbf{r}+\mathbf{r}_p)\right)\right]d^3\mathbf{r}_e\right\} \\
&\approx \frac{\partial}{\partial\mathbf{E}_{\text{ext}}(\mathbf{r})}\left\{-\int_\Omega\sum_j^{\text{valence}}\frac{1}{e}\nu_j\psi_j^*(\mathbf{r}_e;\mathbf{r})\psi_j(\mathbf{r}_e;\mathbf{r})\nabla\left[\sum_{\mathbf{r}_p}\left(-\frac{Z^{\text{full}}_{\text{Al}}e^2}{|\mathbf{r}_e-\mathbf{r}-\mathbf{r}_p|}\right)\right]d^3\mathbf{r}_e\right\} \\
&\quad + \frac{\partial}{\partial\mathbf{E}_{\text{ext}}(\mathbf{r})}\left\{-\int_\Omega\sum_j^{\text{core}}\frac{1}{e}\nu_j\psi_j^*(\mathbf{r}_e;\mathbf{r})\psi_j(\mathbf{r}_e;\mathbf{r})\nabla\left[\sum_{\mathbf{r}_p}\left(-\frac{Z^{\text{full}}_{\text{Al}}e^2}{|\mathbf{r}_e-\mathbf{r}-\mathbf{r}_p|}\right)\right]d^3\mathbf{r}_e\right\} \\
&= \frac{Z^{\text{full}}_{\text{Al}}}{Z^{\text{valence}}_{\text{Al}}}\frac{1}{e}\frac{\partial\mathbf{F}^{\text{valence}}_{\text{Al}}}{\partial\mathbf{E}_{\text{ext}}(\mathbf{r})} + \delta_{\text{core}} = \vec{Z}'''_{\text{Al static wind}}(\mathbf{r}) + \delta_{\text{core}},
\end{aligned} \tag{A5}$$

where

$$\delta_{\text{core}} = \frac{\partial}{\partial\mathbf{E}_{\text{ext}}(\mathbf{r})}\left\{-\int_\Omega\sum_j^{\text{core}}\frac{1}{e}\nu_j\psi_j^*(\mathbf{r}_e;\mathbf{r})\psi_j(\mathbf{r}_e;\mathbf{r})\times\nabla\left[\sum_{\mathbf{r}_p}\left(-\frac{Z^{\text{full}}_{\text{Al}}e^2}{|\mathbf{r}_e-\mathbf{r}-\mathbf{r}_p|}\right)\right]d^3\mathbf{r}_e\right\} \tag{A6}$$

is expected to be small because of the insensitivity of the core orbitals to the external field. The numerical differentiations in Eqs. (24) and (25) were performed by using a series of $\mathbf{F}^{\text{full}}_{\text{Al}}(\mathbf{r})$ or $\mathbf{F}^{\text{valence}}_{\text{Al}}(\mathbf{r})$ under $\mathbf{E}_{\text{ext}}(\mathbf{r})$, by means of the conventional five-point formula

$$f'(x) = \frac{1}{12h}\{f(x-2h) - 8f(x-h) + 8f(x+h) - f(x+2h)\}, \tag{A7}$$

with $h = 1.414\times10^{-3}$ a.u. (7.2723×10^8 V/m).

*Author to whom correspondence should be addressed. E-mail address: akitomo@kues.kyoto-u.ac.jp

[1] J. K. Howard and R. F. Ross, Appl. Phys. Lett. **18**, 344 (1971).
[2] I. A. Blech and E. Kinsbron, Thin Solid Films **25**, 327 (1975).
[3] J. R. Black, IEEE Trans. Electron Devices **ED-16**, 338 (1969).
[4] L. E. Levin, G. Reiss, and D. A. Smith, Phys. Rev. B **48**, 858 (1993).
[5] Y.-C. Joo and C. V. Thompson, J. Appl. Phys. **81**, 6062 (1997).
[6] I. A. Blech, J. Appl. Phys. **47**, 1203 (1976).
[7] C. V. Thompson and J. R. Loyd, Mater. Res. Bull. **18**, 19 (1993).
[8] H. Kawasaki, M. Gall, D. Jawarani, R. Hernandez, and C. Capasso, Thin Solid Films **320**, 45 (1998).

[9] C. Bosvieux and J. Friedel, J. Phys. Chem. Solids **23**, 123 (1962).
[10] A. K. Das and R. Peierls, J. Phys. C **6**, 2811 (1973).
[11] A. K. Das and R. Peierls, J. Phys. C **8**, 3348 (1975).
[12] R. S. Sorbello, J. Phys. Chem. Solids **34**, 937 (1973).
[13] R. S. Sorbello and B. Dasgupta, Phys. Rev. B **16**, 5193 (1977).
[14] P. R. Rymbey and R. S. Sorbello, Phys. Rev. B **21**, 2150 (1980).
[15] R. Landauer and J. W. F. Woo, Phys. Rev. B **10**, 1266 (1974).
[16] R. Landauer, Phys. Rev. B **16**, 4698 (1977).
[17] A. Lodder, J. Phys. F: Met. Phys. **14**, 2943 (1984).
[18] A. Lodder and J. P. Dekker, in *Stress Induced Phenomena in Metallization*, edited by Okabayashi *et al.* (American Institute of Physics, New York, 1998), pp. 315–328.
[19] R. S. Sorbello, Solid State Phys. **51**, 159 (1998).
[20] A. Tachibana, in *Stress Induced Phenomena in Metallization*, edited by S. P. Baker (American Institute of Physics, New York, 2002), pp. 105–116.
[21] K. Doi, K. Nakamura, and A. Tachibana, Appl. Surf. Sci. (to be published).
[22] R. P. Feynman, Phys. Rev. **56**, 340 (1939).
[23] K. Iguchi and A. Tachibana, Appl. Surf. Sci. **159–160**, 167 (2000).
[24] A. Tachibana, Int. J. Quantum Chem. Symp. **21**, 181 (1987).
[25] A. Tachibana, Int. J. Quantum Chem. **35**, 361 (1989).
[26] A. Tachibana, Theor. Chem. Acc. **102**, 188 (1999).
[27] A. Tachibana and R. G. Parr, Int. J. Quantum Chem. **41**, 527 (1992).
[28] A. Tachibana, Int. J. Quantum Chem. **57**, 423 (1996).
[29] A. Tachibana, J. Chem. Phys. **115**, 3497 (2001).
[30] A. Tachibana, in *Reviews in Modern Quantum Chemistry: A Celebration of the Contributions of Robert Parr*, edited by K. D. Sen (World Scientific, Singapore, 2002), Chap. 45, pp. 1327–1366.
[31] A. Tachibana, in *Fundamental Perspectives in Quantum Chemistry: A Tribute to the Memory of Per-Olov Löwdin*, edited by E. Brandas and E. Kryachko (Kluwer Academic Publishers, Dordrecht, in press).
[32] J. M. Ziman, in *Principle of the theory of solids*, edited by J. M. Ziman (Cambridge University Press, Cambridge, 1972), pp. 215–220.
[33] J. P. Perdew and Y. Wang, Phys. Rev. B **45**, 13 244 (1992).
[34] J. P. Perdew, J. A. Chevary, S. H. Vosko, K. A. Jackson, M. A. Pederson, D. J. Singh, and C. Fiolhais, Phys. Rev. B **46**, 6671 (1992).
[35] H. J. Monkhorst and J. D. Pack, Phys. Rev. B **13**, 5188 (1976).